Xu et al. Nanoscale Research Letters (2018) 13:195
https://doi.org/10.1186/s11671-018-2604-4

Nanoscale Research Letters

NANO EXPRESS Open Access

Effect of Zinc Acetate Concentration on Optimization of Photocatalytic Activity of *p*-Co_3O_4/*n*-ZnO Heterostructures

Hongyan Xu[1], Mingliang Shi[1], Caiqin Liang[1], Siyan Wang[1], Chengkai Xia[1], Chenyang Xue[2], Zhenyin Hai[3] and Serge Zhuiykov[1,3*]

Abstract

In this work, *p*-Co_3O_4/*n*-ZnO heterostructures were fabricated on Ni substrate by hydrothermal-decomposition method using cobaltous nitrate hexahydrate ($Co(NO_3)_2{\cdot}6H_2O$) and zinc acetate dihydrate ($Zn(CH_3COO)_2{\cdot}2H_2O$) as precursors with zinc acetate concentration varying from 5.0 to 55.0 mM. Structure and morphology of the developed samples were characterized by X-ray diffraction (XRD), Raman spectroscopy, and scanning electron microscopy (SEM). Effect of zinc acetate concentration on the photocatalytic activity of *p*-Co_3O_4/*n*-ZnO heterostructures was investigated by degradation of methyl orange (MO) under the UV light irradiation. The fabricated *p*-Co_3O_4/*n*-ZnO heterostructures exhibited higher photocatalytic activity than pure Co_3O_4 particles. In order to obtain the maximum photocatalytic activity, zinc acetate concentration was optimized. Specifically, at 35 mM of zinc acetate, the *p*-Co_3O_4/*n*-ZnO showed the highest photocatalytic activity with the degradation efficiency of MO reaching 89.38% after 72 h irradiation. The improvement of photocatalytic performance of *p*-Co_3O_4/*n*-ZnO heterostructures is due to the increased concentration of photo-generated holes on Co_3O_4 surface and the higher surface-to-volume ratio in the hierarchical structure formed by nano-lamellas.

Keywords: Co_3O_4/ZnO, Heterostructures, Photocatalysis, Hydrothermal decomposition

Background

The rapid development of various industries at the beginning of the twenty-first century has been leading to the fast growing of wastewater at the speed which never been observed in the past. The consequent deterioration of the water quality has been greatly affecting the health of aquatic ecosystems and vast majority of people living in such ecosystems. Hence, the effective water treatment has become one of the major global concerns for the time being [1]. Several modern technologies including physical, chemical, and bio-chemical methods have been developed for the efficient water treatment [2, 3]. Among them, the photocatalysis process has recently gained great attention due to the superior properties of the developed semiconductor catalysts, which have been utilized for the efficient decomposition of various organic pollutants into the smaller and less harmful substances such as CO_2, H_2O, and organic short-chain acids [3–8]. Specifically, various micro- and nano-structured semiconductors, such as TiO_2, MnO_2, SnO_2, WO_3, Fe_2O_3, Co_3O_4, and ZnO, and different range of their heterojunctions are utilized as functional photocatalysts for the water treatment [9–28]. It is obvious that different photocatalysts have their own benefits and drawbacks. For example, TiO_2 is so far the most widely employed photocatalyst effective against a wide range of microorganisms co-existing in water. However, it can only absorb UV light for its wide bandgap [12, 13]. On the contrary, ZnO is low cost and nontoxic, but possesses rapid recombination of photo-induced electron-hole pairs [29]. Fe_2O_3 has short hole diffusion length (2–4 nm), poor conductivity, and charge recombination [30].

Generally speaking, photocatalysis is based on the reaction between adsorbed molecules (oxygen, surface

* Correspondence: serge.zhuiykov@ugent.be
[1]School of Materials Science and Engineering, North University of China, Taiyuan 030051, People's Republic of China
[3]Department of Applied Analytical and Physical Chemistry, Ghent University Global Campus, 119 Songdomunhwa-ro, Yeonsu-gu, Incheon 21985, South Korea
Full list of author information is available at the end of the article

hydroxyls groups) or water and photo-generated electron/hole pairs excited by the photon with equal or higher energy than the bandgap of semiconductor. However, the electron/hole recombination is blamed for the low quantum yields, which is still a big obstacle for the photocatalytic activity improvement. In order to overcome this obstacle, the development of efficient *p-n* heterojunctions has been proposed and attempted with the different levels of success during last few years. For instance, it was found that the fabricated *p-n* heterojunctions could effectively reduce the recombination rate of the photo-generated electron/hole pairs, which subsequently enhanced the overall photocatalytic activity [31, 32]. Thus, the combination of *p*- and *n*-type semiconductor oxides has paved the way for further development of the *p-n* heterojunctions and optimization of their photocatalytic activity [33].

As an intrinsic *p*-type semiconductor, cobalt oxide (Co_3O_4) has been used in the different photocatalytic applications owing to its chemical stability, nontoxicity, low cost, environmental friendliness, etc. [34]. It was reported that Co_3O_4 with specific band structure can adsorb oxygen much more efficiently compared to the other *p*-type oxide semiconductors [35]. Other strategies, i.e., doping and heterojunctions, have been developing recently in order to improve the photocatalytic efficiency and properties of the doped Co_3O_4-based catalysts such as Co_3O_4/Bi_2WO_6 [36], Co_3O_4/TiO_2 [37], and Bi_2O_3/Co_3O_4 [38] have been reported. On the other hand, ZnO (wide bandgap *n*-type semiconductor) has also been intensively studied as one of the best photocatalytic materials due to its high photochemical activity, nontoxic nature, and relatively low cost. Moreover, it was reported that its photocatalytic activity could also be enhanced significantly by modifying its textural characteristics [39]. Therefore, the combination of *p*-type Co_3O_4 and *n*-type ZnO represents the right approach for successful development of *p-n* heterojunctions as these heterojunctions can provide built-up inner electric field at the *p-n* interface that can subsequently enhance the overall photocatalytic activity of fabricated composite material. In fact, several different approaches and synthesizing methods for fabrication of these *p*-Co_3O_4/*n*-ZnO heterojunctions have recently been reported with reasonable performances [39–41]. However, the optimization of photocatalytic activity of fabricated *p-n* heterostructure, which could be linked to the specific micro- or nano-structural variations, to the best of our knowledge, has rarely been addressed.

In this work, *p*-Co_3O_4/*n*-ZnO heterostructures were fabricated by hydrothermal decomposition method using cobaltous nitrate hexahydrate ($Co(NO_3)_2{\cdot}6H_2O$) and zinc acetate dihydrate ($Zn(CH_3COO)_2{\cdot}2H_2O$) as precursors. Their photocatalytic performance was investigated by taking methyl orange (MO) as an example under the UV light irradiation. The developed *p*-Co_3O_4/*n*-ZnO heterostructures showed enhancement of the photocatalytic activity in degradation of MO compared to the single Co_3O_4 component, as they facilitated more photocatalytic sites and accelerated the surface electron transfer rate due to their much higher surface-to-volume ratio. In addition, the effect of zinc acetate concentration on the photocatalytic activity of *p*-Co_3O_4/*n*-ZnO heterostructures was comprehensively investigated and their photocatalytic activity was optimized.

Results and Discussion

Characterization of Heterostructures

Figure 1 schematically illustrates the fabrication process of *p*-Co_3O_4/*n*-ZnO heterostructures on the Ni substrate. Figure 2 depicts the XRD patterns of the precursor, as-fabricated Co_3O_4 and Co_3O_4/ZnO-35 heterostructures. The diffraction peaks located at 2θ of 44.44°, 51.77°, and 76.31° attributed to (111), (200), and (220) planes, respectively, of Ni (JCPDS card no. 65-2865) observed in all samples [42]. It was found that all identical peaks of the precursor (Fig. 2a) match perfectly to the hexagonal phase of $Co(OH)_2$ (JCPDS card no. 30-0443) [43]. The other diffraction peaks at $2\theta = 19.06°$, 32.47°, 37.92°, 38.66°, 51.36°, and 57.91° corresponded to the (001), (100), (101), (002), (102), and (110) planes of $Co(OH)_2$, respectively. In the Co_3O_4 XRD pattern, the identical $Co(OH)_2$ peaks disappeared and new peaks emerged at 31.27°, 36.85°, 44.81°, 55.66°, 59.35°, and 65.23° were attributed and indexed to the crystal planes (220), (311), (400), (422), (511), and (440) of the cubic spinel phase of Co_3O_4 (JCPDS card no. 43-1003), respectively [44]. These measurements indicated that pure Co_3O_4 is derived from the $Co(OH)_2$ after 2 h heating at 250 °C.

XRD pattern of the developed *p*-Co_3O_4/*n*-ZnO heterostructure shows that the intensities of diffraction peaks for both Ni substrate and Co_3O_4 decreased, which could be caused by the new substance loaded on the surface. In addition, a double-peak can be observed at $2\theta = 36.5°$. Figure 2b displays the partially enlarged pattern of Co_3O_4/ZnO, in which (101) peak of ZnO and (311) peak of Co_3O_4 are clearly separated. This fact unambiguously confirmed the successful synthesis of the *p*-Co_3O_4/*n*-ZnO heterostructures. Moreover, no diffraction impurity peak was detected, which also indicated that the synthesized heterostructures are only made of Co_3O_4 and ZnO.

Figure 3 shows typical Raman spectra of the pure Co_3O_4 and the fabricated *p*-Co_3O_4/*n*-ZnO heterostructure taken at the room temperature. In these Raman spectra, five different Raman active modes $A_{1g} + 3F_{2g} +$

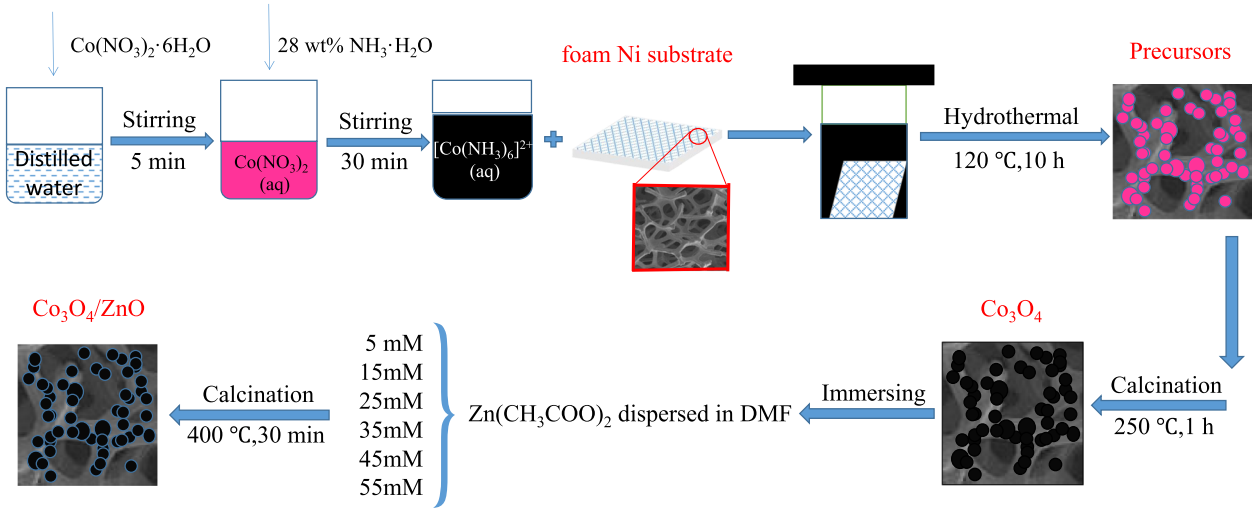

Fig. 1 Schematic representation of the fabrication process of *p*-Co_3O_4/*n*-ZnO heterostructures

E_g of the Co_3O_4 could be observed. It is well known that Co_3O_4 has a spinel structure $Co^{2+}(Co^{3+})_2O^{2-}{}_4$ with Co^{2+} and Co^{3+} positioned at tetrahedral and octahedral sites, respectively [45]. A_{1g} mode is a characteristic of the octahedral sites, and the E_g and F_{2g} modes are related to the combined vibrations of tetrahedral site and octahedral oxygen motions [46]. Even though, there is no obvious ZnO modes appeared in Co_3O_4/ZnO composite, a clear red-shift and broadening features of Co_3O_4 Raman modes presented in the spectrum of Co_3O_4/ZnO heterostructure. The most intense peak A_{1g} varies from 688.9 cm^{-1} in pure Co_3O_4 to 679.7 cm^{-1} in Co_3O_4/ZnO heterostructure, and its full-width at half maximum (FWHM) changes from 14.61 cm^{-1} in pure Co_3O_4 to 16.02 cm^{-1} in Co_3O_4/ZnO heterostructure. These variations are attributed to the coupling between Co_3O_4 and ZnO and also indicated the successful development of Co_3O_4/ZnO heterojunction. The same phenomena have been observed in Raman spectra of graphene covered on Ag nanoparticles [47].

The FTIR spectra of pure Co_3O_4 and Co_3O_4/ZnO heterostructures are presented in Fig. 4. The peaks centered at about 3452 and 1634 cm^{-1} are attributed to the O–H stretching and bending modes of the hydrated oxide surface and the adsorbed water [48, 49]. The IR absorption peaks at about 660 and 568 cm^{-1} confirm the formation of the phase of spinel Co_3O_4 [50]. Compared with the FTIR spectrum of Co_3O_4 nanoparticle, new peak at 432 cm^{-1} appears in all Co_3O_4/ZnO FTIR spectra, which is attributed to the existence of ZnO [51]. In addition, the characteristic peak of ZnO at 432 cm^{-1} becomes sharper with the increasing concentration of zinc source, which confirms the coexistence of ZnO and Co_3O_4 and verifies the successful synthesis of ZnO on the Co_3O_4 nanoparticles.

The surface morphology of the precursor and as-prepared pure Co_3O_4 are presented in Fig. 5. From the low-magnification SEM image of the $Co(OH)_2$ precursor, it is clearly visible that the flower-like layers of precursor, consisting of many sunflower-seed-like petals, have grown uniformly on the surface of the Ni substrate (Fig. 5a). The "petal" size was approximately 10 μm in length, and the whole surface of the porous Ni substrate was covered by $Co(OH)_2$ precursor. Furthermore, low-magnification SEM image (Fig. 5b) depicts that the synthetized Co_3O_4 crystals are also uniformly and densely covered the porous Ni substrate. High-magnification SEM image (Fig. 5c) shows highly dense structure with lots of "sunflower-seed like" Co_3O_4 crystal stacked together to form Co_3O_4 spheres. A single sphere size was approximately ~ 20 μm in length. The "sunflower-seed-like" crystals indicated the morphological hereditability of the Co_3O_4 from its precursor.

The morphologies of Co_3O_4/ZnO heterostructures, which were fabricated with the different zinc acetate concentrations, were also investigated by SEM, and the main results are summarized in Fig. 6. It is clear evidenced from this figure that the changes in zinc acetate concentration during preparation of Co_3O_4/ZnO heterostructures play the crucial role in the development of the morphology variations. For example, the morphology of Co_3O_4/ZnO-5 (Fig. 6a) is very similar to the morphology of pure Co_3O_4 (Fig. 5c), as the concentration of zinc acetate is low. However, as the concentration of zinc acetate increased from 5.0 to 25.0 mM, the crystallization of sunflower-seed-like small crystals intensified as presented in Fig. 6b, c. What is also interesting is that the size of the sunflower-seed-like crystals

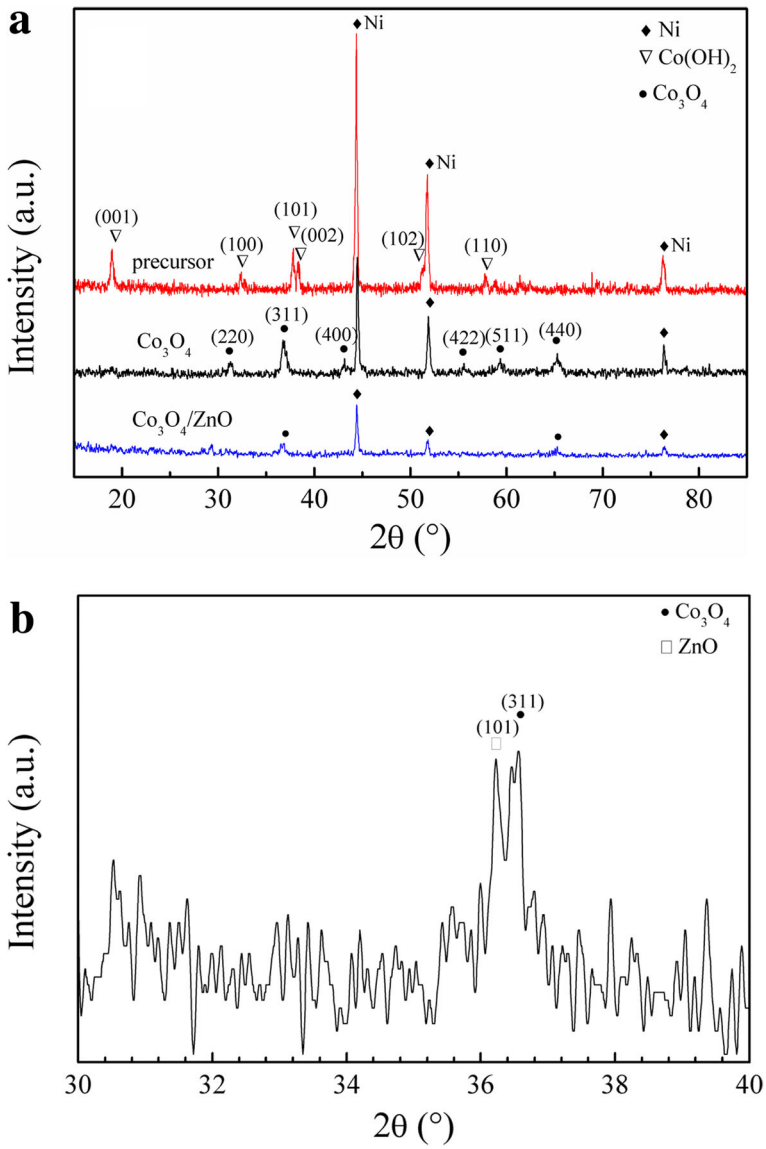

Fig. 2 **a** XRD patterns of the precursor, as-prepared pure Co_3O_4 and Co_3O_4/ZnO-35 heterostructure. **b** Partially enlarged view of the diffraction peaks of Co_3O_4/ZnO-35

appeared to be smaller in Co_3O_4/ZnO-25 than that in Co_3O_4/ZnO-15. Noteworthy, as the zinc acetate concentration increased further to 35.0 mM during fabrication of Co_3O_4/ZnO heterostructures, sunflower-seed-like crystals completely disappeared and the morphology of Co_3O_4/ZnO-35 represented hierarchical spheres (Fig. 6d). It was discovered that the inner part of Co_3O_4/ZnO sphere is assembled by the numerous nano-lamellas with thickness of 100–200 nm, as clearly indicated by the higher resolution SEM image in Fig. 7. The nano-lamellas are stacked together along the radial direction in interpenetrating network to form Co_3O_4/ZnO heterostructural spheres, which ultimately provided higher surface-to-volume ratio in this particular morphology. It is worthwhile to note that as zinc acetate concentration increased further to 45.0 mM, the sunflower-seed-like Co_3O_4/ZnO crystals reappeared again in smaller sizes and the new morphology of Co_3O_4/ZnO is established (Fig. 6e). In this morphology, Co_3O_4/ZnO nanorods have a diameter of approximately 700 nm. Thus, two kinds of crystal morphologies, sunflower-seed-like and nanorod crystals coexisted in Co_3O_4/ZnO-45 heterostructure. Finally, when the zinc acetate concentration reached 55.0 mM, the proportion and the size of Co_3O_4/ZnO rods increased significantly accompanied by their heavy agglomeration (Fig. 6f).

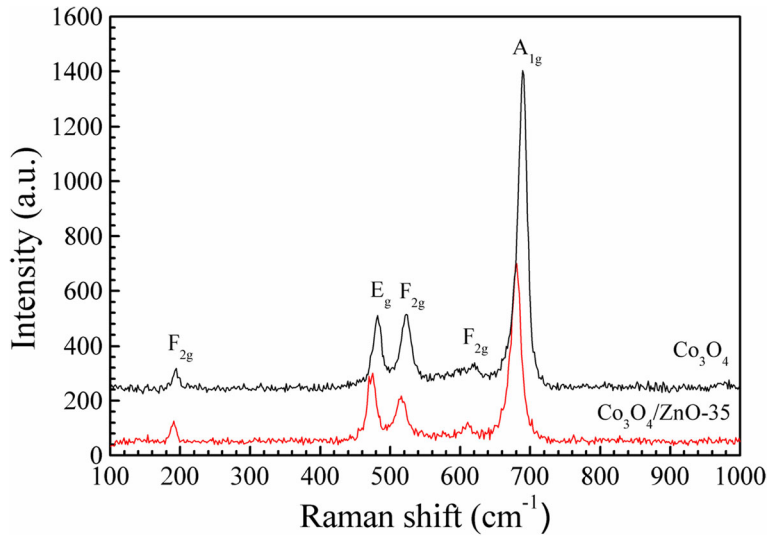

Fig. 3 Raman spectra of pure Co_3O_4 and Co_3O_4/ZnO-35 heterostructure

The elemental Zn, O, and Co in pure Co_3O_4 and Co_3O_4/ZnO heterostructures were detected by EDX, and the corresponding weight and atomic percentages for all samples are listed in Table 1. It is evident that the amount of zinc in Co_3O_4/ZnO heterostructures increases with the increasing concentration of zinc acetate. The elemental mappings of Co, Zn, and O in the Co_3O_4/ZnO-35 heterostructure are displayed in Fig. 8. It can be found that the Co, Zn, and O elements are concomitant and homogeneously distributed in the heterostructure.

Consequently, all the above material characterization techniques signify the successful and uniform development of the Co_3O_4/ZnO heterostructures. Thus, these *p*-Co_3O_4/*n*-ZnO heterostructures were formed without any impurity by the decomposition of $Co(OH)_2$ and zinc acetate $Zn(CH_3COO)_2$ precursors calcined and annealed at 250 and 400 °C, respectively, by the following reactions [52, 53]:

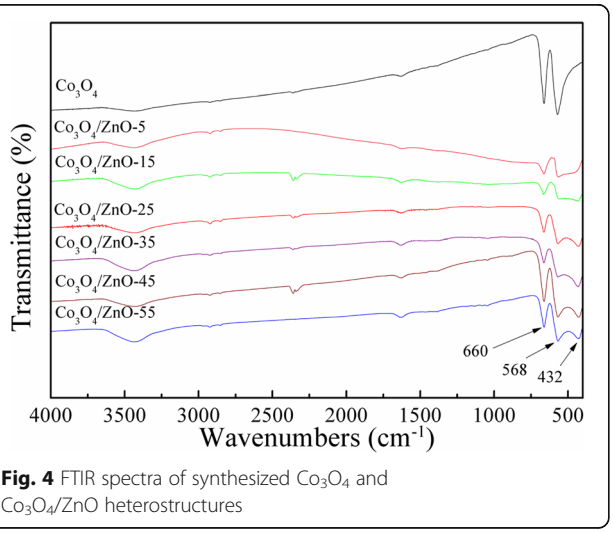

Fig. 4 FTIR spectra of synthesized Co_3O_4 and Co_3O_4/ZnO heterostructures

$$Co^{2+} + 6\,NH_3 \rightarrow \left[Co(NH_3)_6\right]^{2+} \quad (1)$$

$$2\left[Co(NH_3)_6\right]^{2+} + O_2 \underset{\Delta}{\overset{RT}{\rightleftharpoons}} \left[(NH_3)_5CoO_2(NH_3)_5\right]^{4+} + 2\,NH_3\uparrow \quad (2)$$

$$\left[Co(NH_3)_6\right]^{2+} + 2\,OH^- \xrightarrow{\Delta} Co(OH)_2\downarrow + 6\,NH_3\uparrow \quad (3)$$

$$6\,Co(OH)_2 + O_2 \xrightarrow{250^{\circ}C} Co_3O_4 + 6H_2O \quad (4)$$

$$Zn(CH_3COO)_2{\cdot}2\,H_2O \xrightarrow{\Delta} Zn(CH_3COO)_2 + 2\,H_2O \quad (5)$$

$$Zn(CH_3COO)_2 \xrightarrow{400^{\circ}C} ZnO + CH_3COCH_3 + CO_2\uparrow \quad (6)$$

The BET surface areas of pure Co_3O_4 nanoparticles and Co_3O_4/ZnO heterostructures are presented in Table 2, and the corresponding nitrogen adsorption–desorption isotherms are depicted in Figure S1 of Additional file 1. With an increase of the zinc acetate concentration in the developed Co_3O_4/ZnO heterostructures, the BET surface area of samples initially increased and then decreased. For instance, the BET surface area of Co_3O_4/ZnO heterostructure reached to the largest level of 60.23 m^2/g at the zinc acetate concentration of

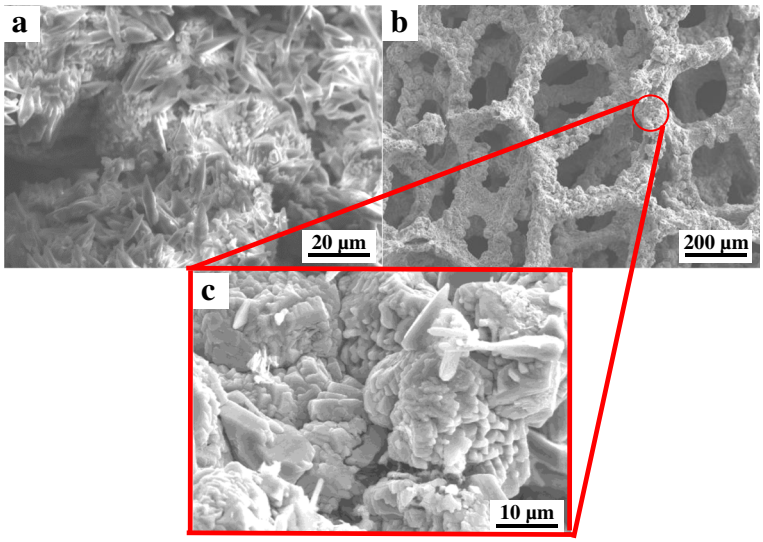

Fig. 5 SEM images of **a** $Co(OH)_2$ precursor and pure Co_3O_4 in **b** low magnification and **c** high magnification

35.0 mM. Larger surface area with more adsorption centers is more beneficial for the degradation of organic dyes [54].

To get further confirmation of the development p-Co_3O_4/n-ZnO heterostructures, part of the Co_3O_4/ZnO-35 structure was peeled off from the Ni substrate to perform XPS analysis. XPS measurements were performed to investigate the chemical binding states of the developed p-Co_3O_4/n-ZnO heterostructure. Figure 9 shows the results of XPS measurements, which were carried out to investigate the chemical binding states of the developed p-Co_3O_4/n-ZnO heterostructure. Figure 9a depicts the oxidation states of Co 2p in the XPS spectrum. Two main peaks Co $2p_{3/2}$ and Co $2p_{1/2}$ were clearly determined at 780.28 and 795.76 eV, respectively. Noteworthy, owing to complete coating of the porous Ni substrate, some noise level has been recorded at Co $2p_{1/2}$. In addition, the Zn 2p spectrum was also recorded during XPS measurements for p-Co_3O_4/n-ZnO heterostructure and this spectrum is presented in Fig. 9b. Two peaks for Zn 2p were also identified as Zn $2p_{3/2}$ and Zn $2p_{1/2}$ at binding energies of 1021.8 and 1044.9 eV, respectively. These results were in the line with other survey [39]. Figure 9c illustrates the O 1s regions for the p-Co_3O_4/n-ZnO heterostructure. Employing the Shirley background two deconvoluted Lorentzian-Gaussian peaks were obtained in O 1s spectrum. These peaks for p-Co_3O_4/n-ZnO heterostructure were clearly pronounced at 530.2 and 531.4 eV, respectively. The recorded peaks are comparable to the other peaks reported for lattice oxygen and chemisorbed oxygen of the surface hydroxyls [41, 55].

Photocatalytic Activity

The photocatalytic degradation of MO under the UV light irradiation ($\lambda = 254$ nm) was carried out at room temperature to evaluate the photocatalytic activity of the developed Co_3O_4 and p-Co_3O_4/n-ZnO heterostructures and specify the effect of zinc acetate concentration on the performance of p-Co_3O_4/n-ZnO heterostructures. The temporal spectral changes of MO aqueous solutions are displayed in Fig. 10. The corresponding relative concentration of MO with irradiation time and the performance of various p-Co_3O_4/n-ZnO heterostructures towards the MO degradation are presented in Fig. 11. As clearly visible from Fig. 10a, MO shown only negligible degradation with increasing irradiation time without catalysts and the degradation efficiency after 72 h of UV irradiation was only 11.66% (Fig. 11a). ZnO also shown poor photocatalytic activity (Figure S2 of Additional file 1). Pure Co_3O_4 demonstrated slightly better photocatalytic activity and the degradation efficiency was ~ 17.64% after 72 h irradiation (Fig. 11a). On the contrary, for the developed p-Co_3O_4/n-ZnO heterostructures utilized as catalysts, the main characteristic absorption peak ($\lambda = 465$ nm) of MO decreased with the increase of the irradiation time (Fig. 10c–h), which caused significant MO degradation. The first-order plot was fitted with this experiment, and the rate constant of MO degradation was obtained by the following equation

$$\ln(C_0/C_t) = kt, \tag{7}$$

where t is the irradiation time, C_0 is the initial concentration at time $t = 0$, C_t is the concentration at time t, and k is the first-order rate constant. As can be observed

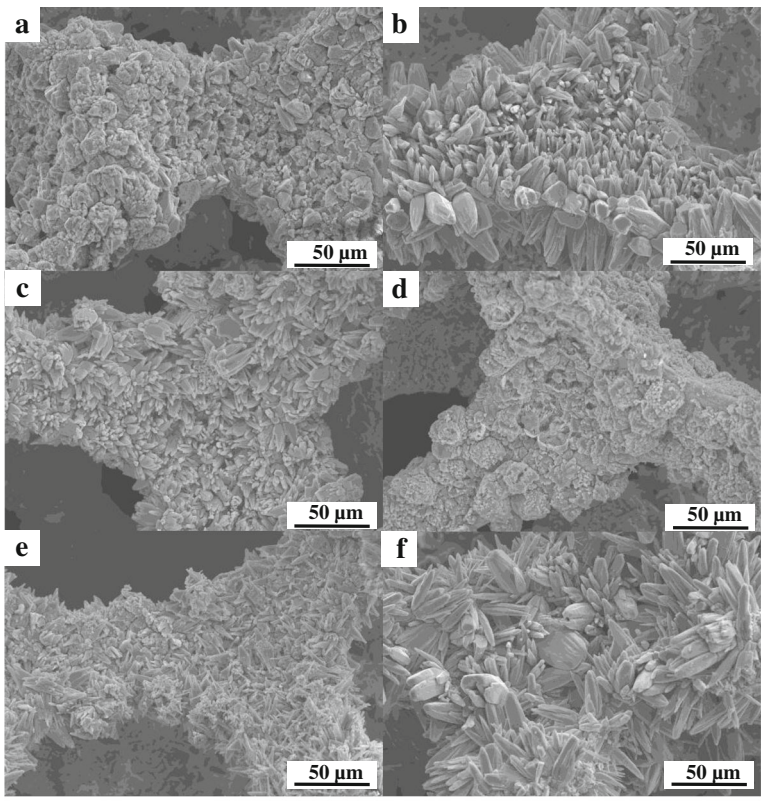

Fig. 6 SEM images of *p*-Co_3O_4/*n*-ZnO heterostructures grown on the surface of Ni substrate: **a** Co_3O_4/ZnO-5, **b** Co_3O_4/ZnO-15, **c** Co_3O_4/ZnO-25, **d** Co_3O_4/ZnO-35, **e** Co_3O_4/ZnO-45, and **f** Co_3O_4/ZnO-55, respectively

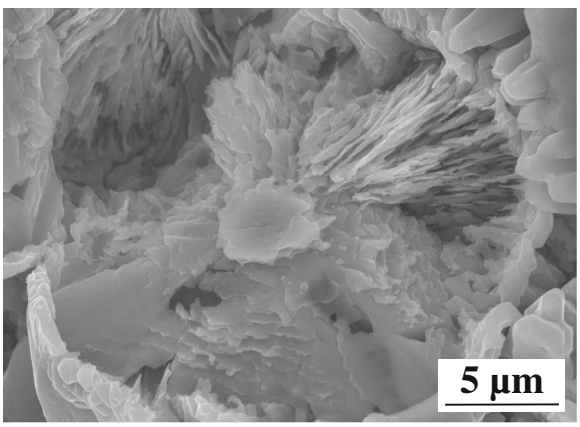

Fig. 7 SEM image of the internal structure of Co_3O_4/ZnO-35

in Fig. 11c, the computed rate constants for Co_3O_4 and *p*-Co_3O_4/*n*-ZnO heterostructures are summarized in Table 3.

The photocatalytic degradation of dyes mainly involves several active radical species such as hydroxyl radicals (·OH), holes (h^+), and electrons (e^-) [29]. In order to investigate the active species in the photocatalytic process to better understand the mechanism of photocatalysis, a series of scavengers were employed during the photo-degradation processes. Isopropanol (IPA), triethanolamine (TEOA), and silver nitrate ($AgNO_3$) were used as scavengers for hydroxyl radicals (·OH), photo-generated holes, and electrons in degradation of MO, respectively [55–57]. The concentration of the three kinds of scavengers was 10 mM. Figure 12 shows the photocatalytic degradation of MO over Co_3O_4/ ZnO-35 heterostructure catalyst was 74.30, 30.55, and 90.25% with 10 mM

Table 1 Weight and atomic percentages of elements in Co_3O_4 nanoparticles and Co_3O_4/ZnO heterostructures detected by EDX

Sample	Co_3O_4		Co_3O_4/ZnO-5			Co_3O_4/ZnO-15			Co_3O_4/ZnO-25			Co_3O_4/ZnO-35			Co_3O_4/ZnO-45			Co_3O_4/ZnO-55		
Element	Co	O	Zn	Co	O	Zn	Co	O	Zn	Co	O	Zn	Co	O	Zn	Co	O	Zn	Co	O
Wt.%	66.16	33.84	1.30	70.06	28.64	1.55	69.67	28.78	1.57	70.40	28.03	2.13	69.64	28.23	2.35	66.54	31.11	5.29	64.51	30.20
Atom%	34.67	65.33	0.66	39.64	59.70	0.79	39.34	59.87	0.81	40.21	58.98	1.09	39.67	59.24	1.16	36.31	62.53	2.64	35.74	61.62

IPA, TEOA, and $AgNO_3$, respectively. This result means the photo-generated holes play much more important roles in MO degradation process, compared to ·OH and photo-generated electrons.

Photoluminescence (PL) technique is widely used to investigate the recombination rate of the photo-induced electron-hole pairs in photocatalyst. Figure 13 shows the room temperature PL spectra of the synthesized Co_3O_4, ZnO, and Co_3O_4/ZnO-35 heterostructure (PL spectra of all samples are presented as Figure S3 in Additional file 1). There are two peaks in the PL spectra of Co_3O_4, ZnO, and Co_3O_4/ZnO heterostructures: one is called near band edge emission (NBE), which is in UV region and due to the recombination of free excitons through an exciton–exciton collision process; and the other one is called deep level emission (DPE, in visible region), which is caused by the impurities and structural defects in the crystal [58, 59]. The DPE intensity in Co_3O_4 and Co_3O_4/ZnO-35 heterostructures is much lower than in ZnO, which indicates that the recombination of the photo-generated charge carriers is harder in Co_3O_4 and Co_3O_4/ZnO-35 heterostructures than in ZnO. It has also been demonstrated that the recombination efficiency of photo-induced electron-hole pairs in ZnO can be effectively inhibited by the modification of In_2O_3 for the formation of heterojunction structure [56]. The DPE of Co_3O_4/ZnO-35 is little higher than pure Co_3O_4, and ZnO amount has no regular effect on the recombination rate of photo-generated charge carriers in Co_3O_4/ZnO heterostructures, which may be caused by the small quantity of ZnO and the increasing of defect concentration at the Co_3O_4/ZnO interface. This indicates that the composition of ZnO has little effect on the recombination of photo-generated electrons and holes in Co_3O_4.

For further investigation of photocatalytic activities of catalysts, the photocurrent transient responses of the synthesized Co_3O_4, ZnO, and Co_3O_4/ZnO heterostructures were measured under the visible light. Figure 14 depicts the photocurrent response of the synthesized Co_3O_4, ZnO, and Co_3O_4/ZnO-35 heterostructures. Notably, the photocurrent density of Co_3O_4/ZnO-35 is much higher than that of ZnO and Co_3O_4, which indicated that the Co_3O_4/ZnO-35 has the highest photocatalytic activity [29].

According to the results above, the improvement of photocatalytic activity of Co_3O_4 by additional incorporation of ZnO is mainly caused by two ways. The first

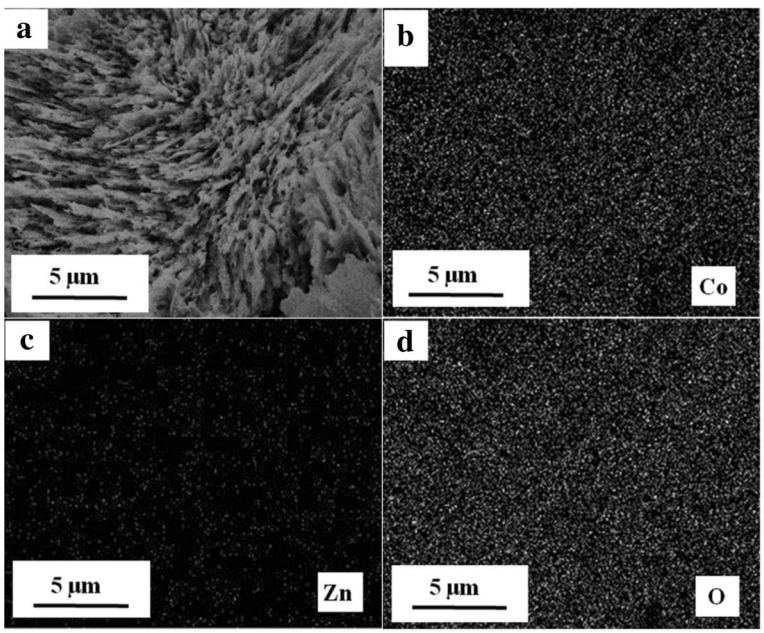

Fig. 8 **a** SEM image of Co_3O_4/ZnO-35 composite with EDX mappings of **b** Co, **c** Zn, and **d** O

Table 2 BET specific surface areas of pure Co_3O_4 nanoparticles and Co_3O_4/ZnO heterostructures

Sample	Co_3O_4	Co_3O_4/ZnO-5	Co_3O_4/ZnO-15	Co_3O_4/ZnO-25	Co_3O_4/ZnO-35	Co_3O_4/ZnO-45	Co_3O_4/ZnO-55
$S_{BET}/m^2 \cdot g^{-1}$	23.97	38.51	40.14	43.48	60.23	26.63	24.19

one is based on the fact that the increasing concentration of photo-generated holes in Co_3O_4 accelerates the photocatalytic rate. As illustrated in Fig. 15, the valence bands (VB) of Co_3O_4 and ZnO are 2.44 V/SHE [60] and 3.03 V/SHE [56], respectively. And the conduction bands (CB) of Co_3O_4 and ZnO are 0.37 V/SHE [60] and − 0.15 V/SHE [56], respectively. After incorporation of *n*-type ZnO the with *p*-type Co_3O_4, the energy levels of Co_3O_4 shift upward, whereas the energy band of ZnO shifts downward until the Fermi energy (E_F) of Co_3O_4 and ZnO reaches an equilibrium. The newly formed energy band structure became to the interactive structure [61]. A large number of *n*-type ZnO nanoparticles are tightly assembled on the surface of *p*-type Co_3O_4. Thus, a large number of nano *p-n* junctions are formed on the surface of Co_3O_4. Under irradiation, both Co_3O_4 and ZnO absorb light and the excited electrons migrate to the CBs whereas the holes remain on the VB of both Co_3O_4 and ZnO. The electrons on the CB of Co_3O_4 could easily transfer to the CB of ZnO. Simultaneously, the holes in the VB of ZnO migrate into the VB of Co_3O_4; thus, the concentration of photo-generated holes on Co_3O_4 surface increases. Based on the data presented in Fig. 12, photo-generated holes play the most important role in photo-degradation process of MO on *p*-Co_3O_4/*n*-ZnO heterostructures. Thus, the increasing concentration of photo-generated holes in the Co_3O_4 VB could lead to its highest photocatalytic activity.

The second way of improvement of photo-catalytic activity is caused by the high-specific surface area of the *p*-Co_3O_4/*n*-ZnO heterostructures. The molecules' absorption-desorption on the surface of catalyst is the first step in degradation process [54, 62]. Consequently, higher surface-to-volume ratio in the developed morphology of *p*-Co_3O_4/*n*-ZnO heterostructures provides more unsaturated surface coordination sites, as shown in Table 2. The *p*-Co_3O_4/*n*-ZnO heterostructures possess higher specific surface area caused by numerous ultrathin nano-lamellas, as confirmed by SEM characterizations. Therefore, high surface-to-volume ratio and suitable interfaces obtained for the Co_3O_4/ZnO-35 heterostructure resulted in its outstanding photocatalytic activity towards the efficient MO degradation.

It needs to note that with the zinc acetate concentration increasing higher than 35.0 mM, the photocatalytic activities of Co_3O_4/ZnO heterostucture decreases. This could be caused by the decrease of their specific surface area (as presented in Table. 2). The similar trend was

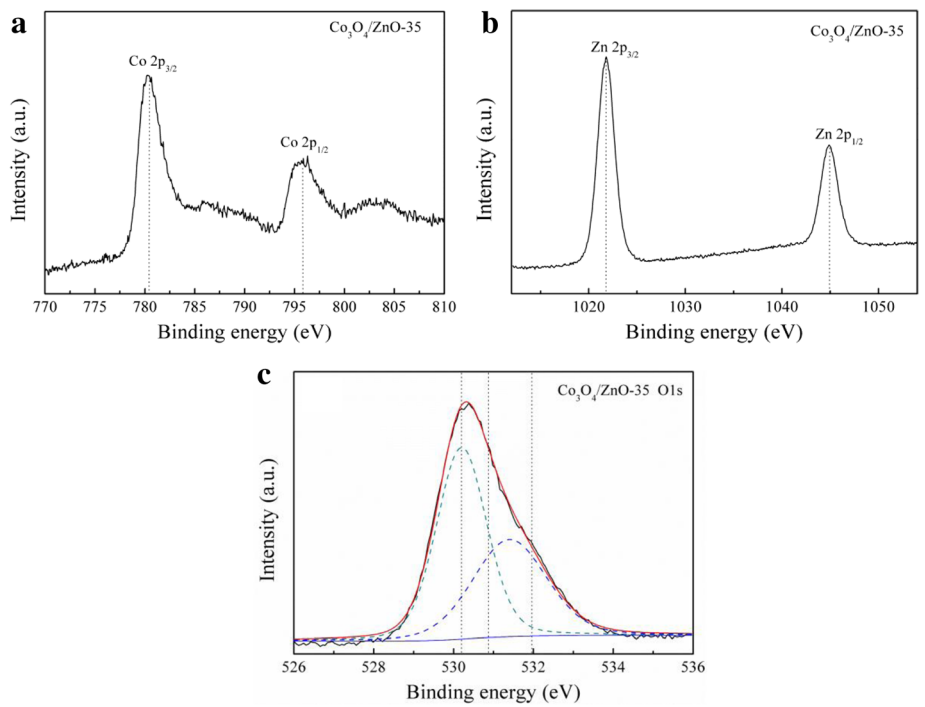

Fig. 9 XPS spectra of **a** Co 2p, **b** Zn 2p, and **c** O 1s of *p*-Co_3O_4/*n*-ZnO heterostructure

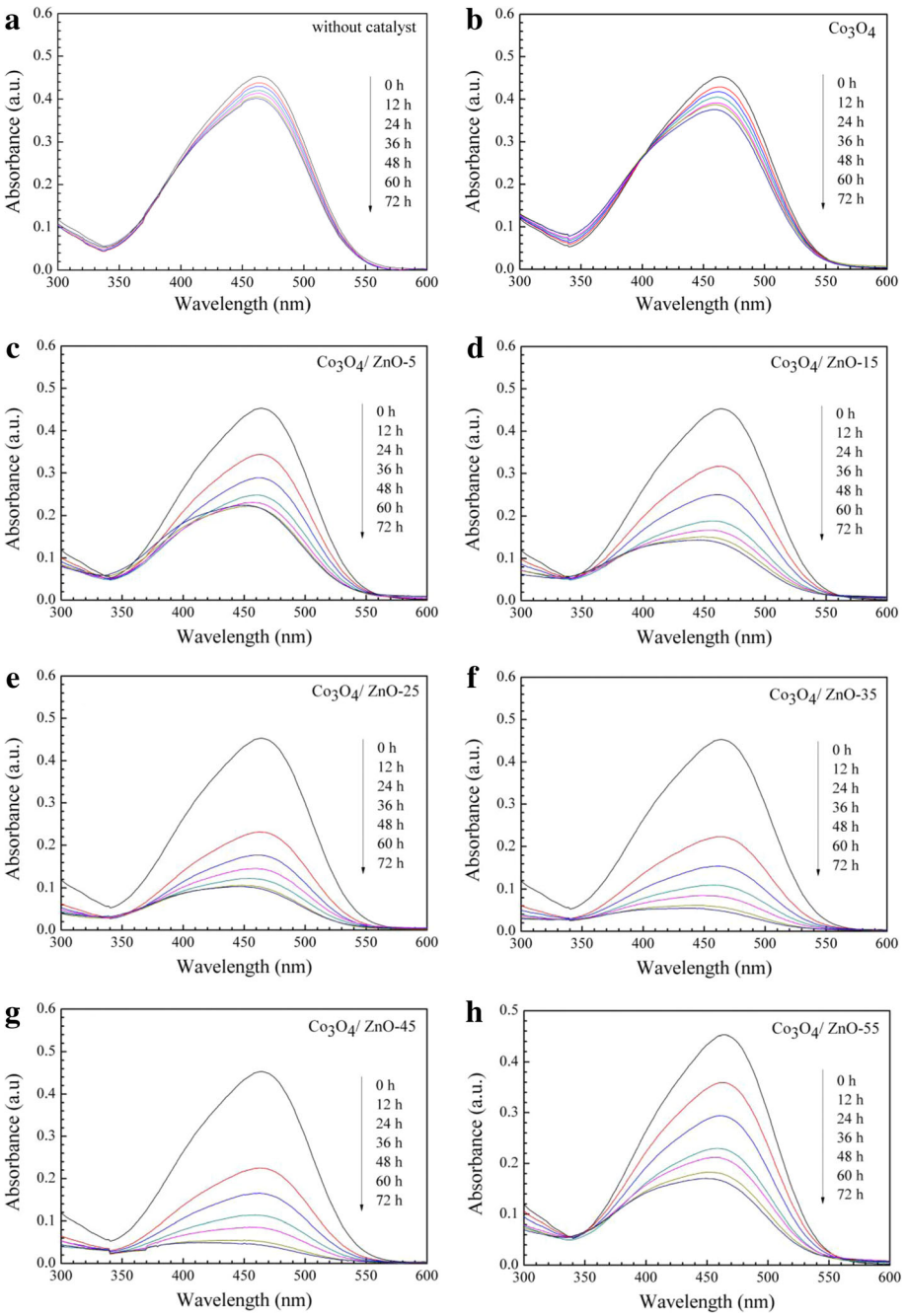

Fig. 10 Irradiation time-dependent UV-vis absorbance spectra of MO aqueous solution: **a** without catalyst, and in the presence of **b** pure Co_3O_4, **c** Co_3O_4/ZnO-5, **d** Co_3O_4/ZnO-15, **e** Co_3O_4/ZnO-25, **f** Co_3O_4/ZnO-35, **g** Co_3O_4/ZnO-45, and **h** Co_3O_4/ZnO-55, respectively

also observed for the tetracycline (TC) degradation by Mn-doped $SrTiO_3$ nanotubes with the increase of Mn dopant concentration [63]. Thus, with certain increase of the zinc acetate concentration, the quantity of ZnO increases and the mass of electron-hole pairs within the space charge region is efficiently separated by the Co_3O_4/ZnO interface resulting in the improvement of MO degradation efficiency.

Noteworthy, the color of both Co_3O_4 and *p*-Co_3O_4/*n*-ZnO heterostructures is not varied from their original one after ~ 72 h of the MO degradation, whereas the color of MO-containing solution faded away from the initial lemon's yellow to almost transparent and even diminished with the Co_3O_4/ZnO-35 heterostructure. FTIR spectrum of Co_3O_4/ZnO-35 heterostructure after 72 h degradation of MO were shown in Fig. 16 (FTIR spectra

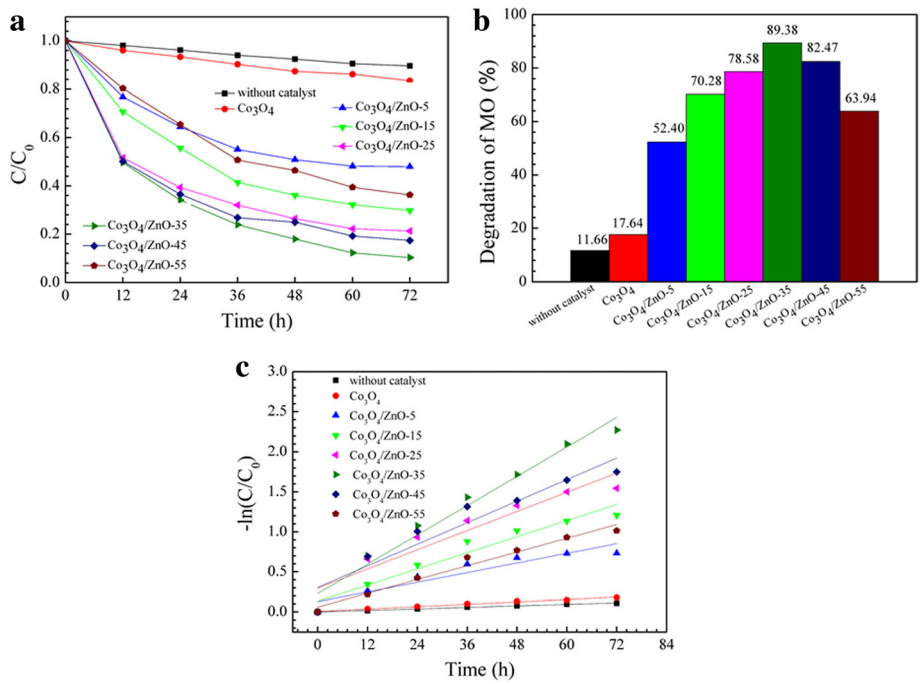

Fig. 11 Photocatalytic activity of pure Co_3O_4 and the different fabricated *p*-Co_3O_4/*n*-ZnO heterostructures: **a** the relative concentration of MO as a function of irradiation time ((C_0 and C are the concentration of MO at initial and any time)), **b** the degradation efficiency of MO in 72 h, **c** first-order plot of MO

of all samples are presented in Figure S4 of Additional file 1). No MO adsorption peak appeared in the FTIR spectrum of Co_3O_4/ZnO-35 heterostructure immersed 72 h in MO solution, indicating that MO molecules are degraded to the smaller molecules [64, 65].

All the above experiments relevant to investigation of the photocatalytic activity of fabricated *p*-Co_3O_4/*n*-ZnO heterostructures undoubtedly confirmed that the MO degradation under the UV light illumination is relatively slow without the presence of catalyst. The presence of *p*-Co_3O_4/*n*-ZnO heterostructures as catalysts significantly increased the rate of MO degradation under the same UV light irradiation conditions. The 35 mM of zinc acetate concentration used in preparation of *p*-Co_3O_4/*n*-ZnO heterostructures has provided the essential prerequisite for development of unique and well-structured morphology with high-surface-to-volume ratio, which subsequently resulted in the maximum photocatalytic activity of the *p*-Co_3O_4/*n*-ZnO heterostructure for the MO degradation. These experimental results indirectly confirmed the fact that the catalytic process was mainly related to the adsorption and desorption of molecules on the large surface area of catalysts. High-surface-to-volume ratio provided more unsaturated surface coordination sites, which in turn endowed *p*-*n* heterojunction with enhanced photocatalytic activity [66].

Conclusions

Different *p*-Co_3O_4/*n*-ZnO heterostructures were successfully fabricated by the hydrothermal decomposition method on the porous Ni substrate with the different zinc acetate concentration varying from 5.0 to 55.0 mM as a ZnO source. The resulted *p*-Co_3O_4/*n*-ZnO heterostructures illustrated various structural morphologies. The synthesized *p*-Co_3O_4/*n*-ZnO heterostructures were subjected to the water treatment as photocatalysts under the UV light irradiation. The reaction rate of MO degradation at the room temperature and at the presence of these photocatalysts was substantially promoted. In fact, *p*-Co_3O_4/*n*-ZnO heterostructures exhibited much higher photocatalytic activity than that of pure Co_3O_4 for MO degradation. It was discovered that the photocatalytic activity of *p*-Co_3O_4/*n*-ZnO heterostructures is greatly affected by the zinc acetate concentration. The optimum zinc acetate concentration was found to be at 35%. At this concentration, the synthesized Co_3O_4/ZnO displayed unique

Table 3 First-order rate constants of pure Co_3O_4 nanoparticles and Co_3O_4/ZnO heterostructures

Sample	methyl orange	Co_3O_4	Co_3O_4/ZnO-5	Co_3O_4/ZnO-15	Co_3O_4/ZnO-25	Co_3O_4/ZnO-35	Co_3O_4/ZnO-45	Co_3O_4/ZnO-55
K (h^{-1})	0.00157	0.00245	0.01004	0.01697	0.01999	0.03054	0.02248	0.01432

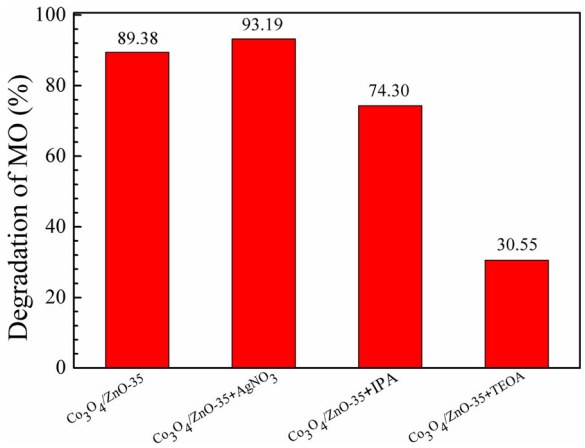

Fig. 12 Trapping experiment of active species during the photocatalytic degradation of MO with Co_3O_4/ZnO-35 under 72 h UV light irradiation

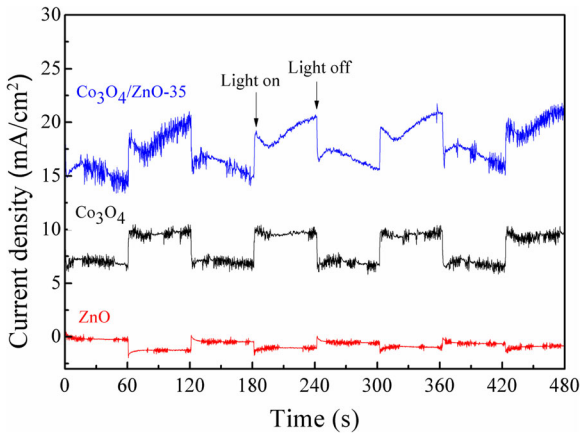

Fig. 14 The photocurrent transient responses profiles for the synthesized Co_3O_4, ZnO and Co_3O_4/ZnO-35 heterostructure

hierarchical nano-lamellar sphere structure and also demonstrated the highest photocatalytic activity among other samples with the different zinc acetate concentration. Co_3O_4/ZnO-35 reached the degradation efficiency of 89.38% for MO decomposition in 72 h of irradiation. With further increase of the zinc acetate concentration, the resulted *p*-Co_3O_4/*n*-ZnO heterostructures demonstrated lower photocatalytic activity towards MO degradation at room temperature. In contrast to the pure Co_3O_4 component, the fabricated *p*-Co_3O_4/*n*-ZnO heterostructures possess higher concentration of photo-generated holes and larger specific surface area, which leads to its enhanced photocatalytic activity.

Methods

Materials Synthesis

All solvents and reagents were purchased from the commercial sources and represented analytical grade. They were used and received without further purification. *p*-Co_3O_4/*n*-ZnO heterostructures were prepared by two-step fabrication method on the porous Ni substrate (25 mm × 25 mm × 1 mm). Initially, the Ni substrates were thoroughly cleaned by acetone and deionized water at the room temperature. Then, they were immersed into 6 M hydrochloric acid and 0.1 M nickel chloride solution for 10 min. After that treatment, the cleaned Ni substrates were dried for further use.

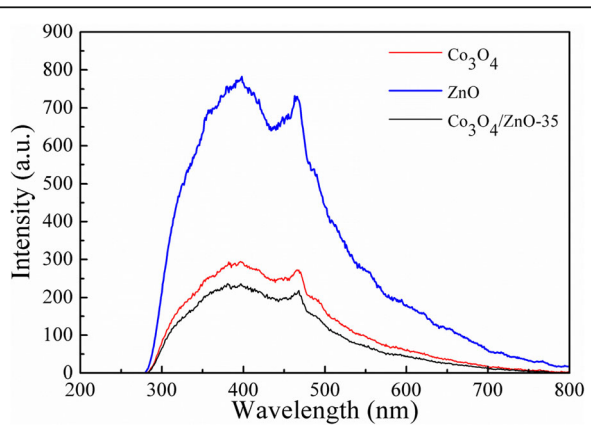

Fig. 13 Room temperature PL spectra of the synthesized Co_3O_4, ZnO, and Co_3O_4/ZnO-35 heterostructure

For fabrication of *p*-Co_3O_4/*n*-ZnO heterostructures on the Ni substrates, 1.7463 g $Co(NO_3)_2{\cdot}6H_2O$ was firstly dissolved in 18 mL of deionized water and stirred for approximately 5 min until the solution turned pink and gradually turned into black by the addition of 12 mL 28 wt.% ammonia solution. pH of solution was 12. Then, both the solution and cleaned Ni substrate were transferred into 50 mL Teflon-lined stainless steel autoclave with subsequent heat-treatment at 120 °C for 10 h. Upon completion of the reaction, the autoclave was cooled to the room temperature and the pH of solution becomes 10.7. The Ni substrate with pink precursor was taken out, washed, and dried with the following calcination at 250 °C for 1 h in ambient air to get Co_3O_4 particles.

At the second step, the Ni substrates with the developed Co_3O_4 particles were immersed for 2 h into zinc acetate $Zn(CH_3COO)_2$ dispersed in N,N–dimethylformamide (DMF) solutions with the different zinc acetate concentrations of 5.0, 15.0, 25.0, 35.0, 45.0, and 55.0 mM, respectively. After that step, the Ni substrates with loaded Co_3O_4/ $Zn(CH_3COO)_2$ structures were dried in air at the room temperature. Finally, they were annealed in the tube furnace at 400 °C for 30 min, the heating rate of 5 °C/min to develop *p*-Co_3O_4/*n*-ZnO heterostructures. The fabricated *p*-Co_3O_4/*n*-ZnO heterostructures obtained at the different zinc acetate concentrations were labeled as Co_3O_4/ZnO-5, Co_3O_4/ZnO-15,

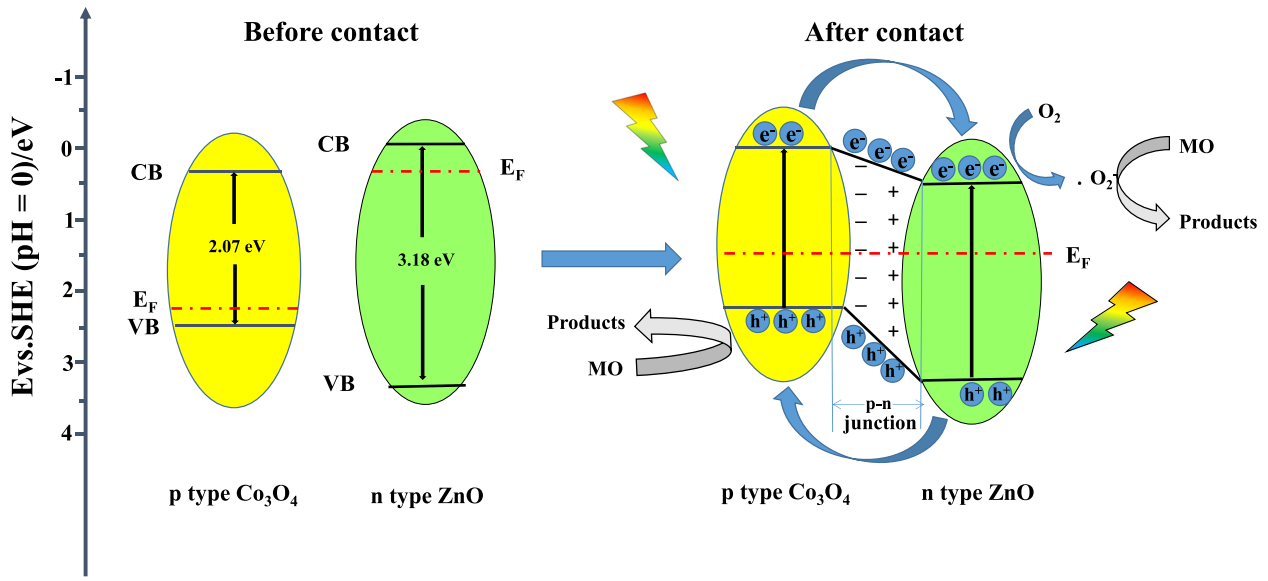

Fig. 15 Schematic diagram of photocatalytic mechanism of Co_3O_4/ZnO-35 composites under UV irradiation

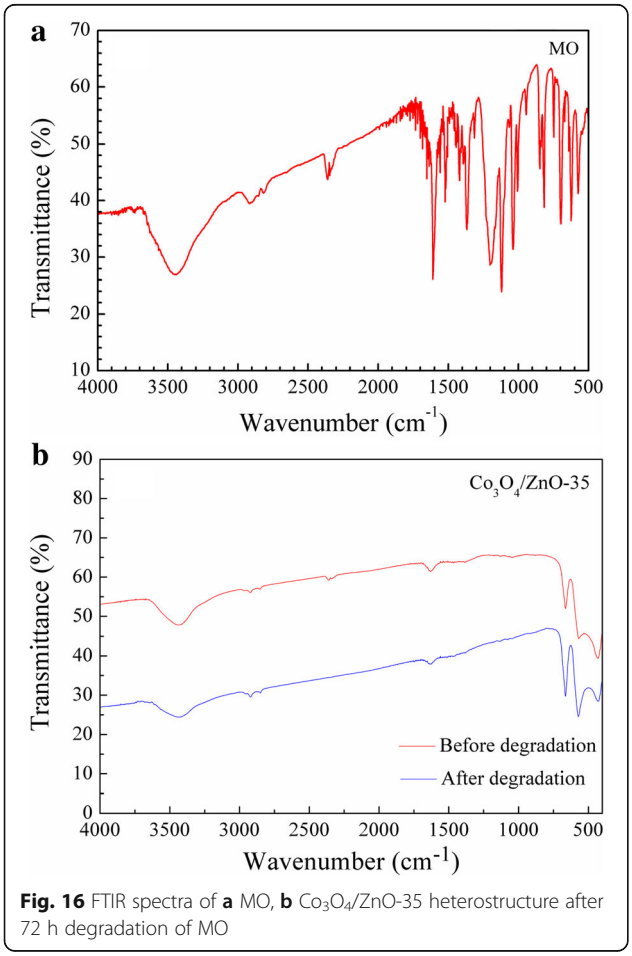

Fig. 16 FTIR spectra of **a** MO, **b** Co_3O_4/ZnO-35 heterostructure after 72 h degradation of MO

Co_3O_4/ZnO-25, Co_3O_4/ZnO-35, Co_3O_4/ZnO-45, and Co_3O_4/ZnO-55, respectively.

Characterization

The crystal structure of precursor, Co_3O_4 particles, and *p*-Co_3O_4/*n*-ZnO heterostructures fabricated on the Ni substrates were characterized by D/Max-rB X-ray diffractometer (XRD) with a Cu-$K_{\alpha1}$ radiation ($\lambda = 0.1542$ nm) operating at 100 mA and 40 kV and a scan rate of 5°/min. Scanning electron microscopy (SEM) and energy dispersive X-ray (EDX) spectroscopy were carried out by a SU-5000 microscope equipped with EDX attachment. The Raman spectra were recorded on a Renishaw in Via Raman microscope, and a 514.5-nm Ar^+ laser line with a power output of 20 mW was used for excitation with a spectral resolution of 2 cm^{-1}. Fourier Transform Infrared (FTIR) spectra were taken using a NEXUS Thermo Nicolet IR-spectrometer in the range 4000–500 cm^{-1} with a spectral resolution of 2 cm^{-1} by KBr disk method. X-ray photoelectron spectroscopy (XPS) was employed in order to investigate the surface chemistries of the developed samples in ESCALAB system with AlK X-ray radiation at 15 kV. All XPS spectra were accurately calibrated by the C 1s peak at 284.6 eV to compensation of the charge effect. Brunauer-Emmett-Teller (BET, JW-BK122F, China) was applied to analyze the specific surface area. Room temperature photoluminescence (PL) spectra of the synthesized Co_3O_4 and *p*-Co_3O_4/*n*-ZnO heterostructures were performed on an F-4600 fluorescent spectrophotometer (Hitachi Corp., Tokyo, Japan), the maximal excitation wavelength was 200 nm, and the filter was 300 nm.

Photocatalytic Activity Evaluation

The photocatalytic activity of both as-fabricated Co_3O_4 and p-Co_3O_4/n-ZnO heterostructures developed on the Ni substrates for the MO ($C_{14}H_{14}N_3NaO_3S$) degradation in aqueous solution under the UV light was evaluated by measuring absorbance of the irradiated solution. For this study, Ni substrates attached with the different p-Co_3O_4/n-ZnO heterostructures were placed into 100 mL of MO solutions with a concentration of 6 mg/L and pH of 6.5. The solutions were continuously stirred in dark for 2 h before illumination in order to reach the absorption-desorption equilibrium between MO and the p-Co_3O_4/n-ZnO heterostructures. Then, the solutions were irradiated by 30 W low-pressure UV lamp ($\lambda = 254$ nm), which was located at the distance of 50 cm above the top of the dye solution. During the process, 5 mL solutions were pipetted every 12 h for the absorbance determination by a UNIC UV-2800A spectrophotometer using the maximum absorbance at 465 nm. All experiments were performed under the ambient condition and room temperature. The degradation efficiency of MO was defined as:

$$D = [(A_0 - A_t)/A_0] \times 100\%, \quad (8)$$

where D is degradation efficiency, A_0 is the initial absorbance of MO solution, and A_t is the absorbance of MO solution after UV irradiation within the elapsed time t.

Photo-Electrochemical Characterization

The photocurrent measurements were carried out at an open circuit potential using an electrochemical workstation (CHI-660e, Chenhua Instrument Corp., China). A three-electrode system was used with the prepared Co_3O_4 or Co_3O_4/ZnO samples, Pt plate, and saturated calomel electrode (SCE) acted as working, counter, and reference electrodes, respectively. A 300 W Xe lamp with an optical filter (AM 1.5 G) was employed as the excitation light source and NaOH solution (1 M) was used as the electrolyte.

Additional File

Additional file 1: Figure S1. Nitrogen adsorption–desorption isotherms of (a) Co3O4, (b) Co3O4/ZnO-5, (c) Co3O4/ZnO-15, (d) Co3O4/ZnO-25, (e) Co3O4/ZnO-35, (f) Co3O4/ZnO-45, and (g) Co3O4/ZnO-55. Figure S2. Irradiation time dependent UV-vis absorbance spectra of MO aqueous solution in the presence ZnO. Figure S3. PL spectra of (a) ZnO, Co3O4, and Co3O4/ZnO heterostructures, and (b) the magnification of the square in (a). Figure S4. FTIR spectra of Co3O4 and Co3O4/ZnO heterostructures after 72 h degradation of MO. (DOCX 779 kb)

Abbreviations

DMF: N,N–dimethylformamide; EDX: Energy dispersive X-ray; FTIR: Fourier transform infrared; MO: Methyl orange; SEM: Scanning electron microscopy; UV–vis: Ultraviolet-visible; XPS: X-ray photoelectron spectroscopy; XRD: X-ray diffraction

Acknowledgements

S.Z. acknowledges the support from the "100 Talents Program" of Shanxi province, People's Republic of China.

Funding

This study was supported and funded by the National Natural Science Foundation of China (grant no. 61501408) and the Shanxi province international cooperation project (grant no. 201703D421008). Research project supported by the Shanxi scholarship council of China (2017-094).

Availability of Data and Materials

The crystal structure and chemical bonding structure of the as-prepared samples were characterized by XRD patterns (Fig. 2), Raman spectra (Fig. 3), XPS (Fig. 8), and FTIR (Fig. 12). The morphologies of the samples were investigated by SEM as shown in Figs. 4, 5, and 6. Photocatalytic tests were examined by UV-vis absorbance spectra (Figs. 9, 10, and 11).

Authors' Contributions

HX, CX, and SZ conceived the idea and designed the growth experiment and investigation process. HX, MS, and CL performed the growth experiments and photocatalytic tests. SW and CX performed XRD and Raman tests and analyzed the results. CX and ZH performed SEM and XPS tests and analyzed the results. HX, MS, CL, and SZ wrote the manuscript. All authors read, discussed, corrected, and approved the final manuscript.

Competing Interests

The authors declare that they have no competing interests.

Publisher's Note

Author details

[1]School of Materials Science and Engineering, North University of China, Taiyuan 030051, People's Republic of China. [2]Key Laboratory of Instrumentation Science and Dynamic Measurement of Ministry of Education, North University of China, Taiyuan 030051, People's Republic of China. [3]Department of Applied Analytical and Physical Chemistry, Ghent University Global Campus, 119 Songdomunhwa-ro, Yeonsu-gu, Incheon 21985, South Korea.

Received: 7 February 2018 Accepted: 15 June 2018
Published online: 05 July 2018

References

1. Shannon MA, Bohn PW, Elimelech M et al (2008) Science and technology for water purification in the coming decades. Nature 452:301–310
2. Torkkeli A (2003) Droplet microfluidics on a planar surface. VTT Publ 61: 3–194
3. Gómez-Pastora J, Dominguez S, Bringas E et al (2017) Review and perspectives on the use of magnetic nanophotocatalysts (MNPCs) in water treatment. Chem Eng J 310:407–427
4. Hai Z, Du J, Akbari MK et al (2017) Carbon-doped MoS_2 nanosheet photocatalysts for efficient degradation of methyl orange. Ionics (Kiel) 23: 1921–1925
5. Pirhashemi M, Habibi-Yangjeh A (2017) Ultrasonic-assisted preparation of plasmonic ZnO/Ag/Ag_2WO_4nanocomposites with high visible-light photocatalytic performance for degradation of organic pollutants. J Colloid Interface Sci 491:216–229
6. Trawiński J, Skibiński R (2017) Photolytic and photocatalytic degradation of tandospirone: determination of kinetics, identification of transformation products and in silico estimation of toxicity. Sci Total Environ 590-591:775–798
7. Jing F, Liang R, Xiong J et al (2017) MIL-68(Fe) as an efficient visible-light-driven photocatalyst for the treatment of a simulated waste-water contain Cr(VI) and Malachite Green. Appl Catal B Environ 206:9–15

8. Akbari MK, Hai Z, Wei Z, Hu J, Zhuiykov S (2017) Wafer-scale two-dimensional Au-TiO_2 bilayer films for photocatalytic degradation of palmitic acid under UV and visible light illumination. Mater Res Bull 95:380–391
9. Agustina TE, Ang HM, Vareek VK (2005) A review of synergistic effect of photocatalysis and ozonation on wastewater treatment. J Photochem Photobiol C Photochem Rev 6:264–273
10. Saiz J, Bringas E, Ortiz I (2014) Functionalized magnetic nanoparticles as new adsorption materials for arsenic removal from polluted waters. J Chem Technol Biotechnol 89:909–918
11. Rivero MJ, Alonso E, Dominguez S et al (2014) Kinetic analysis and biodegradability of the Fenton mineralization of bisphenol A. J Chem Technol Biotechnol 89:1228–1234
12. Pozan GS, Isleyen M, Gokcen S (2013) Transition metal coated TiO_2 nanoparticles: synthesis, characterization and their photocatalytic activity. Appl Catal B Environ 140-141:537–545
13. Daskalaki VM, Antoniadou M, Li Puma G et al (2010) Solar light-responsive Pt/CdS/TiO_2 photocatalysts for hydrogen production and simultaneous degradation of inorganic or organic sacrificial agents in wastewater. Environ Sci Technol 44:7200–7205
14. Sasikala R, Shirole A, Sudarsan V et al (2009) Highly dispersed phase of SnO_2 on TiO_2 nanoparticles synthesized by polyol-mediated route: photocatalytic activity for hydrogen generation. Int J Hydrog Energy 34:3621–3630
15. Kim J, Lee CW, Choi W (2010) Supporting information platinized WO_3 as an environmental photocatalyst that generates OH radicals under visible light. Environ Sci Technol 44:6949–6854
16. Subramonian W, Wu TY, Chai SP (2017) Photocatalytic degradation of industrial pulp and paper mill effluent using synthesized magnetic Fe_2O_3-TiO_2: treatment efficiency and characterizations of reused photocatalyst. J Environ Manag 187:298–310
17. Rosen J, Hutchings GS, Jiao F (2014) Synthesis, structure, and photocatalytic properties of ordered mesoporous metal-doped Co_3O_4. J Catal 310:2–9
18. Chen G, Si X, Yu J et al (2015) Doping nano-Co_3O_4 surface with bigger nanosized Ag and its photocatalytic properties for visible light photodegradation of organic dyes. Appl Surf Sci 330:191–199
19. Edla R, Patel N, Orlandi M et al (2015) Highly photo-catalytically active hierarchical 3D porous/urchin nanostructured Co_3O_4 coating synthesized by Pulsed Laser Deposition. Appl Catal B Environ 166-167:475–484
20. Yusuf S, Jiao F (2012) Effect of the support on the photocatalytic water oxidation activity of cobalt oxide nanoclusters. ACS Catal 2:2753–2760
21. Huang J, Ren H, Chen K, Shim JJ (2014) Controlled synthesis of porous Co_3O_4 micro/nanostructures and their photocatalysis property. Superlattice Microst 75:843–856
22. Kumaresan N, Ramamurthi K, Ramesh Babu R et al (2017) Hydrothermally grown ZnO nanoparticles for effective photocatalytic activity. Appl Surf Sci 418:138–146
23. Xu T, Zhang L, Cheng H, Zhu Y (2011) Significantly enhanced photocatalytic performance of ZnO via graphene hybridization and the mechanism study. Appl Catal B Environ 101:382–387
24. Liang YC, Lung TW, Xu NC (2017) Photoexcited properties of tin sulfide nanosheet-decorated ZnO nanorod heterostructures. Nanoscale Res Lett 12:258–265
25. Hoa NT, Van Cuong V, Lam ND (2018) Mechanism of the photocatalytic activity of p-Si(100)/n-ZnO nanorods heterojunction. Mater Chem Phys 204:397–402
26. Liu H, Hu Y, He X et al (2015) In-situ anion exchange fabrication of porous ZnO/ZnSe heterostructural microspheres with enhanced visible light photocatalytic activity. J Alloys Compd 650:633–640
27. Hao C, Wang W, Zhang R et al (2018) Enhanced photoelectrochemical water splitting with TiO_2@Ag_2O nanowire arrays via p-n heterojunction formation. Sol Energy Mater Sol Cells 174:132–139
28. Iqbal M, Wang Y, Hu H et al (2018) Cu_2O-tipped ZnO nanorods with enhanced photoelectrochemical performance for CO_2 photoreduction. Appl Surf Sci 443:209–216
29. Liu H, Hu C, Zhai H et al (2017) Fabrication of In_2O_3/ZnO@Ag nanowire ternary composites with enhanced visible light photocatalytic activity. RSC Adv 7:37220–37229
30. Chen D, Liu Z, Zhou M et al (2018) Enhanced photoelectrochemical water splitting performance of α-Fe_2O_3 nanostructures modified with Sb_2S_3 and cobalt phosphate. J Alloys Compd 742:918–927
31. Prabhu RR, Saritha AC, Shijeesh MR, Jayaraj MK (2017) Fabrication of p-CuO/n-ZnO heterojunction diode via sol-gel spin coating technique. Mater Sci Eng B Solid-State Mater Adv Technol 220:82–90
32. Wang H, Zhao L, Liu X et al (2017) Novel hydrogen bonding composite based on copper phthalocyanine/perylene diimide derivatives p-n heterojunction with improved photocatalytic activity. Dyes Pigments 137:322–328
33. Li S, Hu S, Xu K et al (2017) Construction of fiber-shaped silver oxide/tantalum nitride p-n heterojunctions as highly efficient visible-light-driven photocatalysts. J Colloid Interface Sci 504:561–569
34. Zhang X, Guo P, Pan Q et al (2017) Novel p-n heterojunction Co_3O_4/AlOOH composites materials for gas sensing at room temperature. J Alloys Compd 727:514–521
35. Nguyen H, El-Safty SA (2011) Meso- and macroporous Co_3O_4 nanorods for effective VOC gas sensors. J Phys Chem C 115:8466–8474
36. Xiao Q, Zhang J, Xiao C, Tan X (2008) Photocatalytic degradation of methylene blue over Co_3O_4/Bi_2WO_6 composite under visible light irradiation. Catal Commun 9:1247–1253
37. Ahmad W, Noor T, Zeeshan M (2017) Effect of synthesis route on catalytic properties and performance of Co_3O_4/TiO_2 for carbon monoxide and hydrocarbon oxidation under real engine operating conditions. Catal Commun 89:19–24
38. Hsieh S-H, Lee G-J, Chen C-Y et al (2013) Hydrothermal synthesis of mesoporous Bi_2O_3/Co_3O_4 microsphere and photocatalytic degradation of orange II dyes by visible light. Top Catal 56:623–629
39. Rubio-Marcos F, Calvino-Casilda V, Bañares MA, Fernandez JF (2010) Novel hierarchical Co_3O_4/ZnO mixtures by dry nanodispersion and their catalytic application in the carbonylation of glycerol. J Catal 275:288–293
40. Dong C, Xiao X, Chen G et al (2014) Hydrothermal synthesis of Co_3O_4 nanorods on nickel foil. Mater Lett 123:187–190
41. Dong C, Xiao X, Chen G et al (2015) Synthesis and photocatalytic degradation of methylene blue over p-n junction Co_3O_4/ZnO core/shell nanorods. Mater Chem Phys 155:1–8
42. Li Y, Hai Z, Hou X et al (2017) Self-assembly of 3D fennel-like Co_3O_4 with thirty-six surfaces for high performance supercapacitor. J Nanomater 2017:1–8
43. Gao L, Xu S, Xue C et al (2016) Self-assembly of hierarchical 3D starfish-like Co_3O_4 nanowire bundles on nickel foam for high-performance supercapacitor. J Nanopart Res 18:1–10
44. Hai Z, Gao L, Zhang Q et al (2016) Facile synthesis of core-shell structured PANI-Co_3O_4 nanocomposites with superior electrochemical performance in supercapacitors. Appl Surf Sci 361:57–62
45. Diallo A, Beye AC, Doyle TB et al (2015) Green synthesis of Co_3O_4 nanoparticles via Aspalathus linearis: physical properties. Green Chem Lett Rev 8:30–36
46. Rashad M, Rüsing M, Berth G et al (2013) CuO and Co_3O_4 nanoparticles: synthesis, characterizations, and Raman spectroscopy. J Nanomater 2013:1–8
47. Zhang SG, Zhang XW, Liu X et al (2014) Raman peak enhancement and shift of few-layer graphene induced by plasmonic coupling with silver nanoparticles. Appl Phys Lett 104:1–5
48. Mahmoud HR, Ibrahim SM, El-Molla SA (2016) Textile dye removal from aqueous solutions using cheap MgO nanomaterials: adsorption kinetics, isotherm studies and thermodynamics. Adv Powder Technol 27:223–231
49. Zhou J, Yang S, Yu J (2011) Facile fabrication of mesoporous MgO microspheres and their enhanced adsorption performance for phosphate from aqueous solutions. Colloids Surf A Physicochem Eng Asp 379:102–108
50. Tang CW, Bin WC, Chien SH (2008) Characterization of cobalt oxides studied by FT-IR, Raman, TPR and TG-MS. Thermochim Acta 473:68–73
51. Djelloul A, Aida M-S, Bougdira J (2010) Photoluminescence, FTIR and X-ray diffraction studies on undoped and Al-doped ZnO thin films grown on polycrystalline α-alumina substrates by ultrasonic spray pyrolysis. J Lumin 130:2113–2117
52. Li Y, Wu Y (2010) Critical role of screw dislocation in the growth of $Co(OH)_2$ nanowires as intermediates for Co_3O_4 nanowire growth. Chem Mater 22:5537–5542
53. Ghule AV, Ghule K, Chen CY et al (2004) In situ thermo-TOF-SIMS study of thermal decomposition of zinc acetate dihydrate. J Mass Spectrom 39:1202–1208
54. Saksornchai E, Kavinchan J, Thongtem S, Thongtem T (2018) Simple wet-chemical synthesis of superparamagnetic CTAB-modified magnetite nanoparticles using as adsorbents for anionic dye Congo red removal. Mater Lett 213:138–142
55. Liu H, Hu Y, Zhang Z et al (2015) Synthesis of spherical Ag/ZnO heterostructural composites with excellent photocatalytic activity under visible light and UV irradiation. Appl Surf Sci 355:644–652
56. Liu H, Zhai H, Hu C et al (2017) Hydrothermal synthesis of In_2O_3 nanoparticles hybrid twins hexagonal disk ZnO heterostructures for

enhanced photocatalytic activities and stability. Nanoscale Res Lett 12: 466–475
57. Zhang J, Zhang L, Shen X et al (2016) Synthesis of $BiOBr/WO_3$ p–n heterojunctions with enhanced visible light photocatalytic activity. Cryst Eng Comm 18:3856–3865
58. Al-Tuwirqi R, Al-Ghamdi AA, Aal NA et al (2011) Facile synthesis and optical properties of Co_3O_4 nanostructures by the microwave route. Superlattice Microst 49:416–421
59. Hu W, Wang L, Wu Q, Wu H (2014) Facile synthesis, magnetic and optical properties of double-shelled Co_3O_4 hollow microspheres. Adv Powder Technol 25:1780–1785
60. Long M, Cai W, Cai J et al (2006) Efficient photocatalytic degradation of phenol over $Co_3O_4/BiVO_4$ composite under visible light irradiation. J Phys Chem B 110:20211–20216
61. Yang C, Gao G, Guo Z et al (2017) Two-step hydrothermal synthesis of novel hierarchical $Co_3O_4/Bi_2O_2CO_3$ p-n heterojunction composite photocatalyst with enhanced visible light photocatalytic activity. Appl Surf Sci 400:365–374
62. Saksornchai E, Kavinchan J, Thongtem S, Thongtem T (2017) The photocatalytic application of semiconductor stibnite nanostructure synthesized via a simple microwave-assisted approach in propylene glycol for degradation of dye pollutants and its optical property. Nanoscale Res Lett 12:589–598
63. Wu G, Li P, Xu D et al (2015) Hydrothermal synthesis and visible-light-driven photocatalytic degradation for tetracycline of Mn-doped $SrTiO_3$ nanocubes. Appl Surf Sci 333:39–47
64. Li P, Song Y, Wang S et al (2015) Enhanced decolorization of methyl orange using zero-valent copper nanoparticles under assistance of hydrodynamic cavitation. Ultrason Sonochem 22:132–138
65. Du L, Wu J, Qin S, Hu C (2011) Degradation mechanism of methyl orange by electrochemical process on RuO_x–PdO/Ti electrode. Water Sci Technol 63:1539–1545
66. Zhu LP, Bing NC, Wang LL et al (2012) Self-assembled 3D porous flowerlike α-Fe_2O_3 hierarchical nanostructures: synthesis, growth mechanism, and their application in photocatalysis. Dalt Trans 41:2959–2965